ARTICLE   OPEN

Check for updates

Electronic fingerprint mechanism of NOx sensor based on single-material SnP3 logical junction

Muhammad S. Ramzan [1,2,3], Agnieszka B. Kuc[1,3 ✉] and Han Seul Kim [4 ✉]

An extraordinary sensing ability of the SnP3-based single-material logical junction for harmful NOx gases was explored in the present work through a set of first-principles electronic structure calculations. As a sensing platform, a metal-semiconductor-metal lateral junction composed of a single material was designed based on the metallic/semiconducting characteristics of trilayer/monolayer SnP3. Lacking a Schottky barrier at the electrode-channel interface, the gas-specific charge transfer between the SnP3 layer and gas molecules was precisely detected based on the current-voltage characteristics. NOx gases with strong adsorption strength and charge transfer amount on the SnP3 substrate were shown to be particularly well detected in this manner, in terms of either the absolute magnitude of the current or negative differential resistance (NDR) at a reasonably small bias voltage as a sensing signal. This work will provide a new pathway to design a Schottky barrier-free metal-semiconductor junction for highly sensitive sensor applications.

INTRODUCTION

Industrialization and available means of transportation are continuously increasing the amount of toxic gases, particularly nitrogen oxides (NOx), in our environment[1]. Due to the increasing demands on devices for indoor air quality control[2], flexible healthcare[3], and gas leak detection[4], the development of high-sensitivity toxic-gas sensors is being actively pursued. Gas sensors can be developed based on various principles, such as semiconducting, catalytic combustion, electrochemical, and gasochromic mechanisms[5,6]. Among others, the semiconducting mechanism is considered particularly promising due to its high sensitivity and low manufacturing cost[7,8].

Two-dimensional (2D) materials have been shown to be very promising candidates for semiconductor-based gas sensors due to their high surface-to-volume ratio and the exceptional ability to modulate the electronic characteristics through doping and functionalization[9–13]. Thus, a wide variety of 2D materials[14–18] with semiconducting properties have been investigated for toxic-gas detection[4,9,19–21]. Along this line, various studies have reported the fabrication of semiconducting-type gas sensors using 2D material-based transistors[19,21–24]. While various 2D materials and device geometries exhibit sensitivity to different gas species, their working mechanisms commonly rely on effective gating through the charge transfer between the 2D materials and gas molecules adsorbed on them.

The basics of the charge transfer between various gas species and novel 2D materials have been well investigated in many simulation studies. Through theoretical studies, MoS_2[22], C_3Si[19], boron-phosphorus[21], $MoSe_2$[23], and WS_2[24] were suggested to be excellent sensing materials for NOx and/or related gases. To theoretically estimate the gas-sensing characteristics based on 2D materials, the non-equilibrium Green's function (NEGF) formalism combined with density functional theory (DFT) simulations is frequently adopted to obtain theoretical current-voltage (*I–V*) curves. This is indeed a very impactful approach in estimating the changes in electrical conduction induced by adsorption-induced charge transfer. By considering the in-plane transport direction of homogeneous semiconducting 2D materials as hypothetical electrode-channel-electrode lateral junctions, variations in the current magnitude due to gas adsorption have commonly been reported. Interestingly, some studies have reported negative differential resistance (NDR) as a characteristic signal of a target gas within a hypothetical semiconductor-only junction, for example, that based on a BP monolayer for NO_2 molecules[21,25,26].

However, directly translating the theoretical estimations of *I–V* curves into the experimental *I–V* characteristics is difficult due to the Schottky barrier (SB) that arises at the interface between metal electrodes and 2D materials. Since the formation of the SB is inevitable when fabricating actual devices, the effective gating of 2D materials due to gas adsorption modulates the SB thickness rather than exhibiting the intrinsic *I–V* curves. Indeed, the SB, which is formed when semiconductors (channels) are brought into contact with metals (electrodes), has been noted as a main bottleneck to large-scale application of 2D material-based logical junctions[27]. In fact, the considerable amount of current dissipation at the channel-electrode interface causes, in general, a great hindrance to realization of semiconductor-based electronic devices.

To overcome this issue, the fabrication of SB-free metal-semiconductor junctions is highly pursued[28–31]. Previously, reducing the contact resistance *via* ion-implantation techniques and the introduction of a semiconducting charge injection layer have been reported[32]. More recently, single-material devices have attracted more attention since their semiconducting channel and metallic electrodes that are constituted by the same material in different phases overcome the complexity and current drop at the electrode-channel interface. The most famous type along this line is the lateral junction based on the semiconducting transition

¹Department of Physics and Earth Sciences, Jacobs University Bremen, Campus Ring 1, 28759 Bremen, Germany. ²Institut für Physik, Carl von Ossietzky Universität Oldenburg, 26129 Oldenburg, Germany. ³Helmholtz-Zentrum Dresden-Rossendorf, Abteilung Ressourcenökologie, Forschungsstelle Leipzig, Permoserstr. 15, 04318 Leipzig, Germany. ⁴Division of National Supercomputing R&D, Korea Institute of Science and Technology Information (KISTI), 245 Daehak-ro, Yuseong-gu, Daejeon 34141, Republic of Korea. ✉email: akuc@hzdr.de; hanseulkim0@kisti.re.kr
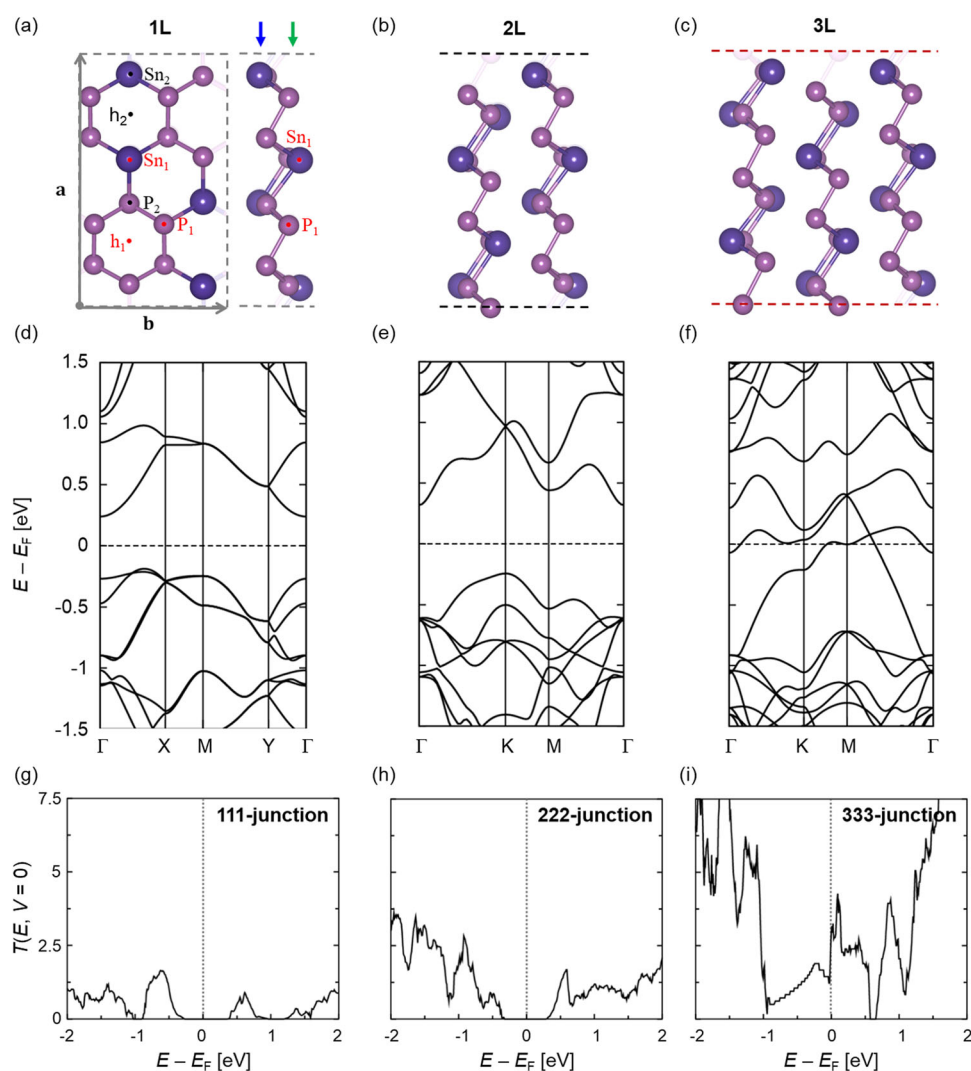
Fig. 1 Crystal structure, electronic band structure, and transport properties of single- and few-layer SnP3. Atomic structures of **a** 1L, **b** 2L, and **c** 3L SnP$_3$ models in a rectangular unit cell representation with lattice vectors **a** and **b**. Each individual layer is composed of two sublayers: upper (green downwards arrow) and lower (blue downwards arrow) layers of Sn and P atoms. h_1, h_2, P_1, P_2, Sn_1, and Sn_2 indicate the possible adsorption sites. In the 2L and 3L models, the layers are stacked in the AB and ABC manner, respectively. **d–f** Corresponding band structures where dashed lines indicate the Fermi levels (E_F). Intrinsic zero-bias tunnelling probabilities of the pristine **g** 111, **h** 222, and **i** 333 SnP$_3$ junction models near the Fermi energy level (E_F). The details for the size of the junctions used to calculate transmission functions are presented in Supplementary Fig. 1. Atom colour code: H–white, C–grey, O–red, N–blue, Sn–purple, and P–light purple.

metal dichalcogenide (TMDC) channel of the 2H phase and locally-induced metallic 1T phase electrode of the same TMDC material[33]. However, the metastable nature of the 1T phase makes fabricating reliable junctions at room temperature difficult.

More recently, 2D materials whose metallic/semiconducting phases can be controlled by the number of vertically stacked layers and SB-free logical junctions based on them have been reported from the simulation point of view. Ghorbani-Asl et al.[34] proposed and simulated the transport properties of a logical junction made of 2H-PdS$_2$ metallic multilayer electrodes and a monolayer (1L) semiconducting channel. Due to the weak van der Waals interaction between each layer of vertically stacked 2D materials, the fabrication of PdS$_2$-based homogeneous logical junctions can be easily realized. Additionally, there has been emerging interest in such noble-metal materials for gas-sensing devices:[34–36]. For example, Teng-Yu et al.[36] successfully synthesized a PtSe$_2$-based gas sensor to detect NO$_2$ gas[36]. However, since the cost of noble metal-based materials might be a bottleneck for commercial use, materials with earth-abundant elements should be developed for

layer-dependent control over metals/semiconductors. Along this line, some previous works, including ours[15,16,37], have recently reported that SnP$_3$ and GeP$_3$ layered materials show quantum confinement effects similar to those of PdS$_2$ and PtSe$_2$, with the 1L and bilayer (2L) being semiconductors and multilayers being metals. Furthermore, recent successful separation of SnP$_3$ nanosheets using liquid-phase exfoliation techniques[38] has motivated us to further investigate SnP$_3$ as a potential single-material gas sensor.

In this work, we investigated from first principles the potential of SnP$_3$ single-material devices for gas-sensing applications involving common pollutants: CH$_4$, CO$_2$, NH$_3$, NO, and NO$_2$. Based on the adsorption energy and corresponding recovery time, we divided the molecules into two categories: type A (non-NO$_x$; CH$_4$, CO$_2$, and NH$_3$) with weak charge transfer and type B (NO$_x$; NO and NO$_2$) with strong charge transfer. The electron transport properties were calculated using trilayer (3L) SnP$_3$ as electrodes and 1L SnP$_3$ as the electron transport channel with respect to gas adsorption. The device showed excellent selectivity for type B NO$_x$ molecules. Different from the cases with type A molecules, the I–V
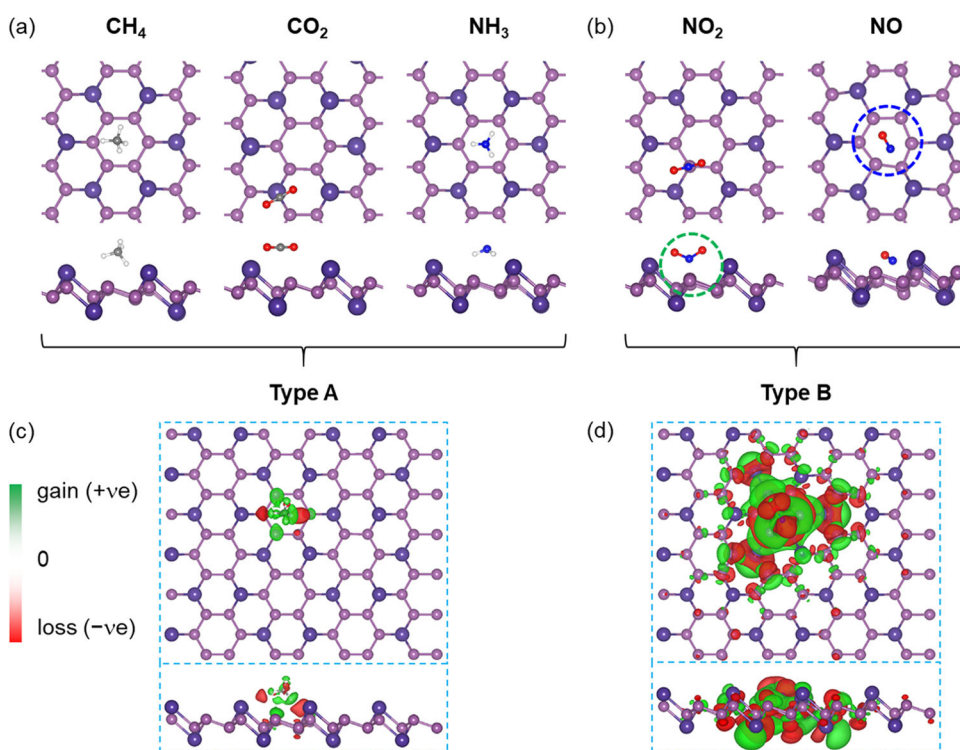
Fig. 2 The most stable configurations and charge density differences of gas molecules on SnP₃ substrate. Top and side views of the energetically most stable configurations of gas molecules of **a** type A and **b** type B adsorbed on 1 L SnP₃. Green and blue circles indicate the NO₂ adsorption through N–P interaction and NO-induced distortions of P₆ ring, respectively. The real-space visualizations of CDDs of **c** type A (CH₄) and **d** type B (NO) cases that are shown to visually compare the absolute magnitude of CDDs between type A and type B. For the cases of CO₂, NH₃, and NO₂, see Supplementary Fig. 4. Green and red areas represent charge accumulation and charge depletion, respectively, with an isovalue of 3×10^{-4} eÅ^{-3}. Atom colour code: H–white, C–grey, O–red, N–blue, Sn–purple, and P–light purple.

characteristics were noticeably reduced with NO₂ adsorption. More interestingly, we observed NDR for the NO molecule within a reasonably small bias voltage range (~ 0.5 V). Therefore, the simulation results strongly suggest that SnP₃ is more sensitive to NO$_x$ than to other gas species. Our results potentially open up a new class of SB-free gas-sensing devices based on single materials that directly utilize the gas-specific modulation of the intrinsic transport properties of the SnP₃ channel.

RESULTS

Structural and electronic properties of pristine single- and few-layer SnP₃

The atomistic models of pristine 1L, 2L, and 3L SnP₃ are shown in Fig. 1a–c. The 1L SnP₃ has a puckered structure with upper and lower sublayers composed of P₆ rings connected by Sn atoms (Fig. 1a). Note that there are six distinguishable adsorption sites for molecular adsorption on the SnP₃ surface by considering the symmetry due to its peculiar structure: h_1 (centre of the P₆ hexagon), h_2 (centre of the P₄Sn₂ hexagon), P_1 (top of the P atom of the upper sublayer), P_2 (top of the P atom of the lower sublayer), Sn_1 (top of the Sn atom of the upper sublayer), and Sn_2 (top of the Sn atom of the lower sublayer). When forming the multilayer, SnP₃ stacks in an ABC ordering (Fig. 1b, c for 2L and 3L SnP₃, respectively). Corresponding band structures are presented in Fig. 1d–f and clearly confirms that 1L and 2L SnP₃ is semiconducting while their 3L SnP₃ counterpart is metallic, as reported in previous works[15,37]. Note that the primary origin of semiconductor-to-metal transition in SnP₃ is the well-known quantum confinement that increases the bandgap when decreasing the number of layers in many 2D materials. Additionally in the case of SnP₃, just as in some other special 2D materials such as

GeP₃[16] and PtSe₂[39,40], its bulk phase shows metallic characteristic due to its particularly strong interlayer coupling energy: an additional valency introduced by the replacement of every fourth P atom with Sn enforces interlayer interaction[16,41]. Thus, the synergetic effect of strong interlayer coupling and strong quantum confinement in SnP₃ results in the layer-dependent metal-to-semiconductor transition. Figure 1f, g, and i show the intrinsic electron transport properties of pristine 1L, 2L, and 3L SnP₃, respectively, by considering each of them as hypothetical in-plane "electrode − scattering region − electrode" junctions (Supplementary Fig. 1). The models are labelled as 111-, 222-, and 333-junctions for 1L, 2L, and 3L SnP₃-based homogeneous junctions, respectively. Being consistent with the band structures, the zero-bias limit ($V = 0$) of the electron transmission functions, $T(E, V = 0)$, indicates that 3L SnP₃ shows gapless metallic electron transport, while its 1L and 2L counterparts are semiconductors with finite energy gaps. This indicates that 3L SnP₃ can be considered a good metal electrode, while 1L/2L SnP₃ can be adopted as a semiconductor channel.

Energetics and electronic structures of the gas-adsorbed SnP₃ substrate

To determine whether the adsorption of distinct gas species results in meaningful differences in the electronic structure of 1L SnP₃, five different molecular species, CH₄, CO₂, NH₃, NO, and NO₂, were considered (Fig. 2a, b). Note that the optimized molecular geometries were obtained as those having minimal adsorption energy (E_{ads}) (see Methods for details) after considering various molecular configurations on all the possible adsorption sites shown in Supplementary Figs. 2 and 3. Interestingly, the gas molecules can be categorized into two types based on the E_{ads} provided in Table 1: type A (CH₄, CO₂, and NH₃; non-NO$_x$) with

Table 1. Details on adsorption configuration, energies, and charge transfer, with corresponding recovery time at room temperature for all gas molecules on 1L, 2L, and 3L SnP₃.

Gas	Conf.	E_{ads}^{1L}	E_{ads}^{2L}	E_{ads}^{3L}	d^{1L}	Δq^{1L}	τ_{300K}^{1L}	τ_{300K}^{2L}	τ_{300K}^{3L}
CH₄	h_1	−0.45	−0.29	−0.30	0.738	0.04	3.04×10^{-5}	8.68×10^{-8}	1.06×10^{-7}
CO₂	Sn_2 (H)	−0.36	−0.37	−0.37	1.766	0.24	1.26×10^{-6}	1.38×10^{-6}	1.91×10^{-6}
NH₃	h_1 (D)	−0.52	−0.35	−0.40	1.088	0.03	6.02×10^{-4}	7.35×10^{-7}	4.58×10^{-6}
NO₂	P_1 (U)	−1.52	−0.97	−1.32	0.657	0.67	3.10×10^{13}	1.66×10^{4}	1.51×10^{10}
NO	h_1 (V)	−1.33	−0.76	−0.94	0.179	0.59	1.82×10^{10}	6.61×10^{0}	6.05×10^{3}

Adsorption configurations (conf.; see Fig. 1, Supplementary Figs. 2 and 3, and I Methods for details) and adsorption energies (E_{ads}, in eV) of gas molecules on 1L, 2L, and 3L SnP₃. Charge transfer amount from 1L SnP₃ to an adsorbed molecule (Δq^{1L}, in e), based on Mulliken charge analysis, and distance (d^{1L}, in Å) between the gas molecule and the nearest atom of the 1L SnP₃ substrate along the plane-normal direction of SnP₃. The recovery times at $T = 300$ K (τ_{300K}) for the 1L, 2L, and 3L cases are also provided. For various τ-values with higher temperatures, see Supplementary Table 1.

weak adsorption of $|E_{ads}| \leq 0.55$ eV and type B (NO and NO₂; NOₓ) with strong adsorption of $|E_{ads}| > 1.30$ eV. Among the type A molecules, the CO₂ molecule prefers the horizontal orientation (H, see Methods) at the Sn_2 site, while CH₄ and NH₃ adsorb on h_1 sites (Fig. 2a). Note that, in contrast to their type A counterparts, type B molecules show extremely small adsorption distances, implying strong N (gas)–P (SnP₃) interactions. Among the type B molecules, NO₂ prefers the P_1 site with the N atom pointing directly to the P atom by stabilizing the system through N–P interaction (green dotted circle in Fig. 2b), while NO favours the h_1 site with a nearly vertical orientation (Fig. 2b). Interestingly, the adsorption of NO on SnP₃ is accompanied by small distortions of the corresponding P_6 ring within the SnP₃ layer (blue dotted circle in Fig. 2b). Such distortion is not observed for the cases with the other molecules. Thus, SnP₃ is expected to possibly offer distinguishable signals, which would be much stronger than the effect of simple charge transfer, for the detection of NOₓ, especially NO molecules.

Simultaneously, the amount of charge transfer between the 1L SnP₃ and the adsorbed molecules (Δq^{1L}) was extracted through Mulliken charge analysis (Table 1). Mulliken analysis shows that electrons were transferred from the substrate to the gas molecule in all cases. Moreover, consistent with what we have obtained with the E_{ads} above, the amount of Δq^{1L} (Table 1) again quantitatively distinguishes type A molecules (CH₄, NH₃, and CO₂) with small or intermediate charge transfer (< 0.25 e) and type B molecules (NO and NO₂) with large charge transfer (> 0.5 e). The spatial distributions of the charge density difference (CDD; see Fig. 2c, d and Supplementary Fig. 4) visualize the adsorption-induced charge transfer. CDD is defined as:

$$\text{CDD} = \rho_{SnP_3+gas} - (\rho_{SnP_3} + \rho_{gas}) \quad (1)$$

where ρ_{SnP_3+gas}, ρ_{SnP_3}, and ρ_{gas} indicate the charge densities of 1L SnP₃ with the adsorbed gas molecule, 1L SnP₃, and the gas molecule, respectively. The CDD shows that the transferred charge is localized for type A molecules around the gas molecule while being delocalized for type B molecules.

Another important property of a gas-sensing material is its recovery time (τ), which indicates the reusability of the SnP₃ substrate. The recovery time can be calculated as follows:

$$\tau = \nu^{-1} \exp \frac{|E_{ads}|}{k_B T} \quad (2)$$

where ν, k_B, and T are the attempt frequency of bond breaking, Boltzmann constant, and temperature, respectively. E_{ads} is the adsorption energy. One of the reference works showing a good recovery time of $\tau = 16$ s for $\nu = 1$ THz at room temperature is based on simulations of NO₂ adsorption on carbon nanotubes[42]. For 2D materials, some experimental works showed $\tau = 150$ s for NH₃ on WS₂ flakes and $\tau = 240$ s for NO on In₂O₃ nanosheets[43,44]. We also adopted the same attempt frequency value, $\nu = 1$ THz, to calculate the room-temperature ($T = 300$ K) recovery times (τ_{300K}).

Our results show layer-dependent recovery times for 1L SnP₃: type A molecules show ultrafast recovery of 3.04×10^{-5} s, 1.26×10^{-6} s, and 6.02×10^{-4} s for CH₄, CO₂ and NH₃, respectively. In fact, the values are rather large for type B molecules: 3.10×10^{13} s and 1.82×10^{10} s for NO₂ and NO, respectively. Thus, additional techniques to reduce the recovery time should be introduced for the practical use of SnP₃ channel for gas sensors. Indeed, recent developments of gas sensors utilize resistive heaters or micro-heaters based on micro electro mechanical systems (MEMS) to achieve high working temperature ($T \gg 300$ K) and efficiently desorb the gas molecules[45]. In this regard, τ values for $T > 300$ K are provided in Supplementary Table 1, reporting that the extracted τ values in this study are comparable to those of the recently developed gas sensors. The values decrease for the case of 2L SnP₃, whereas metallic 3L SnP₃ has a larger τ than the 2L in all cases. This indicate that the 2L SnP₃ channel would provide a better sensing platform than its 1L channel counterpart in terms of response and recovery speed. Note that, however, since we have already observed similar electron transport properties in the 1L and 2L SnP₃ substrates, we will focus only on the 1L SnP₃ channel to reduce the calculation cost in the following parts of this paper.

Gas adsorption-induced changes in quantum transport of semiconducting 111-junction

Then, we observed the gas adsorption-induced changes in the electronic structure and transport properties of the 1L SnP₃ substrate. Figure 3a, b show the projected density of states (PDOS) of SnP₃ with gas adsorption for the cases with type A (Fig. 3a) and B (Fig. 3b) molecules. The figures clearly reveal that the electronic state contributions of the adsorbed molecules are either an infinitesimal amount (CH₄) or located very far from the band edges of SnP₃ (NH₃) for type A molecules. Among the type A molecules, the molecular states of CO₂ are located relatively close to the Fermi level (E_F) compared to those of the other molecules. In contrast, prominent molecular states appear close to E_F (NO) or they are even located at E_F (NO₂) for type B molecules. For the type B molecules, there is noticeably strong hybridization of the electronic states between the molecule and the substrate so that the PDOS of SnP₃ undergoes left-shift in both cases. In particular, while the PDOS of SnP₃ only slightly left-shifted for NO₂, the case with NO shows the noticeable conduction-band filling and correspondingly large E_F shift.

Then, the 111-junction shown in Fig. 3c is constructed to investigate the zero-bias transmission of 1L SnP₃ upon adsorption of molecules of type A (Fig. 3d) and type B (Fig. 3e). While we will focus on 313-junction where the metallic 3L SnP₃ is adopted as the electrode and the semiconducting 1L SnP₃ acts as scattering region in the later part of this paper, investigating the intrinsic transport properties of 111-junction is beneficial to deeply
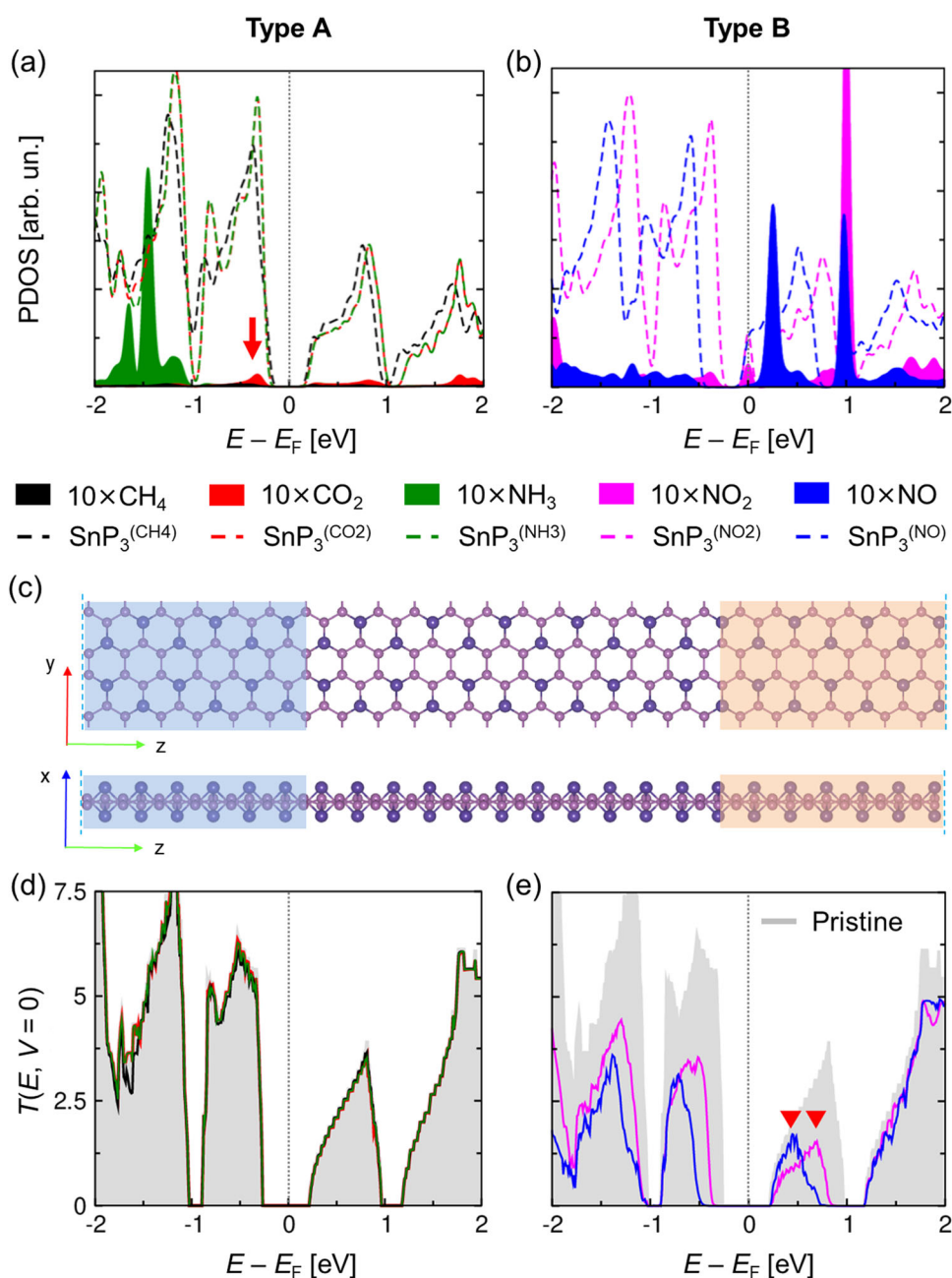
Fig. 3 Electronic structure and transport properties of 111-junction in the presence of gas molecules. PDOS of 1L SnP$_3$ with adsorbed gas molecules of **a** type A and **b** type B. Black, red, green, blue, and magenta colours indicate CH$_4$, CO$_2$, NH$_3$, NO, and NO$_2$, respectively. PDOS for each molecule are marked with colour-filled peaks and were scaled up ten times for visibility. Dashed lines represent the PDOS of the SnP$_3$ substrate for each adsorption model, as indicated by SnP$_3^{(molecule)}$ in the legend. Note that the states of CH$_4$ lie outside the energy range plotted here. The red downwards arrow indicates the electronic state of CO$_2$ near E_F. **c** Top view (top) and side view (bottom) of the device (111-junction) used to calculate the transmission. Blue and orange shaded regions indicate the left and right leads, respectively. Transmission functions for 111-junction with each adsorbed gas molecule with **d** type A and **e** type B molecules, indicated by solid lines with the colour corresponding to those used in PDOS. The $T(E, V = 0)$ of the pristine 111-junction is marked in grey. Note that this model is designed to observe the effect of molecular adsorption on electron transport, so that the dimension of this model is different from what is used in Fig. 1g (Supplementary Fig. 1) with which we compare pristine 111-, 222-, and 333-junctions without molecular adsorption. Furthermore, the model is designed to be also comparable to 3L SnP$_3$ (metal)—1L SnP$_3$ (semiconductor)—3L SnP$_3$ (metal) junction which we will denote as 313-junction in the later part of this paper. In order to accommodate molecules in the scattering region and avoid the possible effects of edge states comes from the 1L-3L SnP$_3$ interfaces, the scattering region in this model is longer by almost two times than what is used in Fig. 1g (Supplementary Fig. 1). The red downward triangles indicate the first transmission peaks above E_F of the 111-junction with NO and NO$_2$ adsorptions. Note that the slight difference between this $T(E, V = 0)$ of pristine 111-junction and Fig. 1g comes from above-mentioned difference in the dimension of atomistic models.
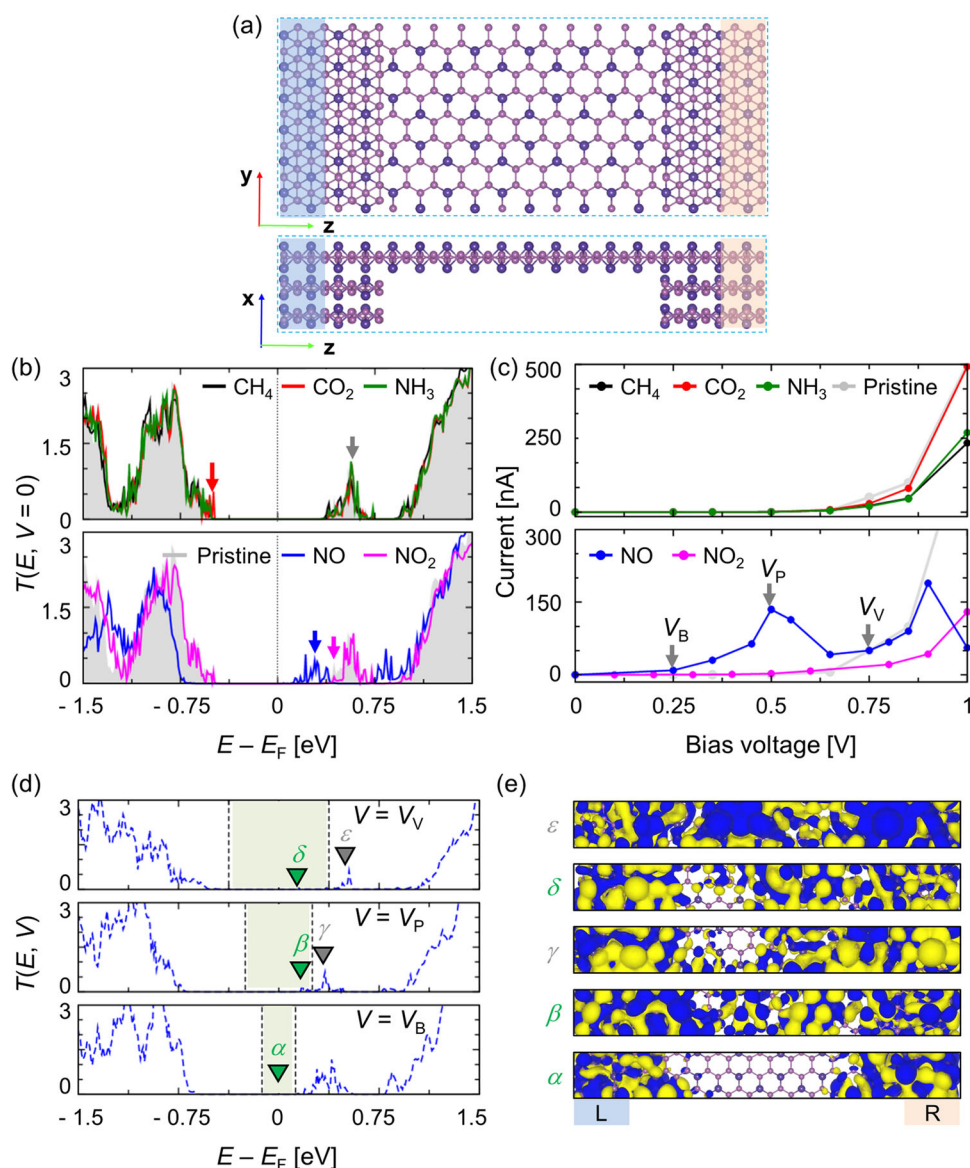
Fig. 4 Zero-bias transmissions and I–V curves of all gas molecules on 313-junction. a Atomic structure of 313-junction with 1L SnP$_3$ transport channel and 3L SnP$_3$ electrodes. The device model is constructed with 3L SnP$_3$ electrodes (highlighted with blue and orange rectangles), overlap regions of 3L SnP$_3$ as buffers, and a 1L SnP$_3$ transport channel. **b** Zero-bias transmission function, $T(E, V = 0)$ of 313-junction with type A (top) and type B (bottom) molecules adsorbed on top of the transport channel ($T(E, V = 0)$ of the pristine SnP$_3$ 313-junction is shown in grey shaded area for comparison), and **c** corresponding I–V curves. Grey, red, blue, and magenta downwards arrows indicate the electronic states originating from SnP$_3$, CO$_2$, and NO, and the NO$_2$-induced suppression of the $T(E, V = 0)$ peak near E_F, respectively. The I–V curve for the pristine 313-junction is marked as grey lines (see Supplementary Fig. 7). Grey downward arrows indicate the three notable bias voltages in describing NDR, namely, base ($V_B = 0.25$ V), peak ($V_P = 0.50$ V), and valley ($V_V = 0.75$ V) points. **d** Bias-dependent transmission functions, $T(E, V)$, for V_B, V_P, and V_V with the case of NO molecule. For each bias, green and grey downwards triangles correspond to the transmission eigenchannel inside and outside of the bias window (marked as the green shaded area), respectively. The eigenchannels are labelled to simplify the convention $E_{\text{bias voltage}}^{\text{eigen energy}}$ as $\alpha\left(E_{0.25\,V}^{0.0\,eV}\right)$, $\beta\left(E_{0.50\,V}^{0.18\,eV}\right)$, $\gamma\left(E_{0.50\,V}^{0.35\,eV}\right)$, $\delta\left(E_{0.75\,V}^{0.15\,eV}\right)$, and $\varepsilon\left(E_{0.75\,V}^{0.52\,eV}\right)$ and are spatially visualized in **e**.

understand the details in 313-junction. Note that 111-junction is prevalently adopted in the field of computational analysis on 2D materials-based gas sensors, as discussed in the introduction section. The values of $T(E, V = 0)$ indicate that the molecules of type A induce only a negligible change in the intrinsic transport properties of the pristine 1L SnP$_3$ (grey area in Fig. 3d, e), which is consistent with what we have seen in the PDOS. Note that such negligible changes in $T(E, V = 0)$ for type A molecules are due to the insignificant hybridization and charge transfer between the molecular and SnP$_3$ electronic states. In contrast, a noticeable reduction of $T(E, V = 0)$ over a wide energy range is observed for

type B molecules, reflecting the strong hybridization and charge transfer between the molecular and substrate electronic states. In both NO and NO$_2$ cases, the valence-band maximum contribution of $T(E, V = 0)$ moves downwards than in pristine 111-junction, in terms of electronic energy. Also, the upper energy bound of the first peak above the E_F also downshifts so that the peak point (indicated by red downward triangles) effectively comes closer to E_F. Note that the effect is particularly strong for the NO molecule due to the strong hybridization of the molecular states. The mechanism behind such reduction and downshift in $T(E, V = 0)$ lies on above-mentioned left-shift of PDOS in type B cases (Fig. 3b).

Since the electrode of 111-junction is semiconductor with a finite bandgap, the meaningful charge transfer between the molecule and SnP_3 in the type B cases results in energy mismatch between electrode and scattering region. This results in the reduction of possible eigenchannel to electron tunnelling, effectively reducing the size of the transmission peaks. The visual explanation on this is provided in Supplementary Fig. 5.

Fingerprint signals of NO_x on the transmission and I–V curve for 313-junction

As we have discussed in the introduction section, constructing a gas-sensing platform that consists of SB-free interfaces is extremely beneficial for direct detection of gas-induced electrical signals. Thus, we here construct a single-material logical junction based on 3L SnP_3 (metal)—1L SnP_3 (semiconductor)—3L SnP_3 (metal) interfaces, as shown in Fig. 4a, which we call a 313-junction (see Methods for details). To investigate the performance of the 313-junction in the electrical detection of gas molecules, zero-bias $T(E, V = 0)$ curves are first obtained, as shown in Fig. 4b. Upon adsorbing type A molecules which shows very small amount of charge transfer with SnP_3 as discussed above, $T(E, V = 0)$ is almost unchanged from that of the pristine 313-junction. To clearly observe the $T(E, V = 0)$ of the pristine 313-junction in comparison to the 111-junction, see Supplementary Fig. 6. The transport peak just above E_F within the 313-junction (grey downwards arrow in Fig. 4b) is very slightly depressed since the type A molecules act as scattering centres rather than additional transport states. The slight $T(E, V = 0)$ peak at $E = E_F - 0.55$ eV (red downwards arrow in Fig. 4b) reflects that the observed PDOS peak in CO_2 below E_F (red downwards arrow in Fig. 3a) indeed contributes to the electron transport in this junction. For type B molecules, the strongest change is again visible for the NO molecule: the valence-band edge contribution and the first peak above E_F of $T(E, V = 0)$ shift to lower energies compared to the cases with the other molecules (blue downwards arrow in Fig. 4b), while a new peak emerges at $E_F + 0.75$ eV. For NO_2, a suppression of the transport peak above E_F is particularly noticeable (magenta downwards arrow in Fig. 4b), indicating that the current flow through the junction would be greatly decreased with the adsorption of NO_2 than that of type A molecules. This is because NO_2 shows stronger hybridizations and charge transfers with SnP_3 (Fig. 3b), so that it acts as stronger scattering centre than its type A molecules counterparts. However, for NO with much stronger hybridization, the electronic states of scattering region would shift toward lower E as discussed in Fig. 3b. Being different from the 111-junction, the metallic electrode of 3L SnP_3 in 313-junction covers such shift so that the $T(E, V = 0)$ peak above E_F is greatly left-shifting (blue downwards arrow in Fig. 4b) rather than disappearing.

To evaluate the gas-sensing performance of the suggested 313 single-device logical junction, I–V curves for the adsorption of different molecules were obtained from the Landauer-Büttiker formula[46] shown in Eq. (5) (see Methods). The curves can be divided into two categories based on their shapes for the bias range up to 1.0 V: (i) the conventional diode-like I–V curve, where the current increases with voltage—obtained for all molecules except NO (Fig. 4c)—and (ii) the I–V curve with NDR, where for some bias values, the current decreases—obtained for the NO molecule. The molecules within the first category show reduced currents compared to that for pristine SnP_3 (grey lines in Fig. 4c), indicating electrical resistance upon molecular adsorption (to clearly observe the I–V curve of the pristine 313-junction, see Supplementary Fig. 7). However, due to the above-mentioned $T(E, V = 0)$ channel in the CO_2 case near the band edge (red downwards arrow in Fig. 4b), the CO_2-adsorbed 313-junction shows almost unchanged I–V characteristics. Noticeably, the NO_2 molecule (lower panel in Fig. 4c) shows a significantly suppressed current magnitude compared to the other molecules as we

expected above, which distinguishes NO_2 from the other molecules in the diode-like I–V curves.

In the most interesting case of the NO molecule, the current first increases to a maximum value of ~150 nA at 0.5 V and then decreases with increasing voltage to ~42 nA at 0.65 V, resulting in NDR (lower panel in Fig. 4c). From that point on, the current again increases to another maximum at 0.90 V and then decreases again. To better understand the NDR for the NO molecule, we analysed the finite-bias transmission function, $T(E, V)$, with respect to different V values (Fig. 4d) and the corresponding scattering eigenchannels (Fig. 4e) at three representative voltage points, marked with downwards arrows in Fig. 4c: namely, the base point (V_B, at 0.25 V), peak point (V_P, at 0.50 V) and valley point (V_V, at 0.75 V). At V_B, well-localized scattering states at α (at 0.0 eV) are present on both electrodes and in the additional overlap region (bottom panel of Fig. 4e) due to the lack of transport eigenchannels within the 0.25 V bias window around E_F. At V_P, due to the additional electronic states in the channel region evolving upon NO adsorption, there is a well-established electrical connection throughout the device, as indicated by the eigenchannel β (at 0.18 eV) inside the bias window. Further increasing the bias voltage to V_V starts to slowly break this connection (eigenchannel δ at 0.15 eV) and causes the current to drop, because the NO-induced electronic state is energetically localized. In contrast, for the pristine 313 junction which is absent of NDR in $V < 1.0$ V, the transport peak at the conduction-band area (grey downward arrow in Fig. 4b) rigidly shift upwards without emerging any new states when increasing V values in $T(E, V)$ (Supplementary Fig. 8). As a result, the tail of the peak smear into the bias window from larger V than the NO-adsorption case. Based on such adsorption-induced modulation of transport eigenchannels, the SnP_3 313-junction particularly well detects NO molecules through the fingerprint NDR characteristics.

DISCUSSION

In summary, we highlight the main points of this work as follows:

- Theoretical suggestion of a new single-material logical junction using SnP_3 that avoids the common "high contact resistance" problem and its device application.
- Step-by-step design and investigation of the working mechanism of a NO_x-sensitive gas sensor based on electrical fingerprints within a single-material logical junction.

In detail, we started with the idea that the layer-dependent electronic properties of SnP_3 can be exploited for single-material logical junctions, overcoming problems arising from electrode-channel junctions such as high SBs. To theoretically suggest its gas sensor applications, several common gases were considered, CH_4, CO_2, NH_3, NO_2, and NO. Throughout a set of first-principles simulations, the molecules were categorized as type A (CH_4, CO_2, and NH_3; non-NO_x) and type B (NO_2 and NO; NO_x) based on their adsorption strength, charge transfer amount, and electronic hybridization with SnP_3. Correspondingly, the electrical signals of a single-material junction (313-junction) where 1L and 3L SnP_3 were used for the transport channel and electrodes, respectively, can distinguish NO_x from non-NO_x molecules by reflecting the electrical interaction between SnP_3 and gas molecules. While the I–V curve of the 313-junction shows only a small change with the adsorption of non-NO_x molecules, a drastic change is observed when adsorbing NO_x molecules. A drastic current drop for NO_2 compared to the other molecules is observed, and more importantly, NO shows an exceptional NDR at a relatively low bias voltage. Thus, the SnP_3 313-junction has sensitivity towards harmful NO_x molecules based on both current depression (NO_2) and NDR (NO) as fingerprint characteristics.

Finally, we would like to mention that this theoretical study focuses on the new idea on gas sensing through the qualitative

feature of NDR, rather than being quantitative. We adopt PBE functional by considering the computational cost related to rather large atomistic model and numerically tough NEGF method in this study, but there is a well-known bandgap underestimation of DFT with PBE functional. Thus, the bandgap of SnP_3 as well as the energy gap between highest occupied molecular orbital (HOMO) and lowest unoccupied molecular orbital (LUMO) is underestimated in this study. We have briefly checked that such bandgap underestimation does not change the qualitative feature, but the exact voltage that NDR appears should not be understood as quantitative feature. Instead, we would like to highlight the concept of Schottky-barrier free SnP_3 single-material junction and qualitative understandings of its molecular sensing property via NO_x-specific electrical signal. We hope this work gives a new insight to the experimentalist as well as computational scientists who studies related topics such as gas sensor or 2D materials-based electrical devices. Furthermore, we expect this work to shed light on the vast applicability of SB-free single-material junctions in general.

METHODS

Atomistic modellings and first-principles calculations

Layered structures (1L, 2L, and 3L) were cut out from bulk SnP_3, which had an $R\overline{3}m$ space group[47]. In each layer of SnP_3, every Sn atom is attached to three P atoms, while each P atom is bound to one Sn and two other P atoms (Fig. 1). The layers are stacked on top of one another in an ABC manner. Each individual layer forms a honeycomb pattern. All layered models were subsequently optimized (atomic positions and lattice vectors) as follows: 2L ($a = b = 7.255$ Å) and 3L ($a = b = 7.283$ Å) were modelled as hexagonal unit cells, while 1L ($a = 7.111$, $b = 12.318$ Å) was modelled as a rectangular unit cell to account for possible atomic reconstruction[15]. We found, however, no reconstruction in the latter. Adsorption of gas molecules and electronic transport calculations were performed on rectangular supercells. As gas molecules, we considered CH_4, CO_2, NH_3, NO, and NO_2, and calculations of the adsorption sites, charge transfer, and CDDs were performed on the 2×3 supercell. Various adsorption sites were considered (cf. Fig. 1a): h_1—middle of the P hexagon, h_2—middle of the P_4Sn_2 hexagon, and P_1 (Sn_1) and P_2 (Sn_2)—on top of the P (Sn) atom of the top (1) and bottom (2) atomic layers, respectively. At each adsorption site, several representative molecular orientations were considered: horizontal (H) and vertical (V) or facing upwards (U) and downwards (D) for linear (CO_2 and NO) or nonlinear (CH_4, NH_3, and NO_2) molecules, respectively (Supplementary Fig. 2).

For geometries and electronic structure calculations, we used DFT as implemented in the SIESTA (Spanish Initiative for Electronic Simulations with Thousands of Atoms) package[48]. We employed double-ζ plus polarization basis sets and Troullier-Martins-type norm-conserving pseudopotentials[49] to describe core electrons, whereas the exchange-correlation potential was treated with the Perdew-Burke-Ernzerhof (PBE) functional of the generalized gradient approximation (GGA)[50]. We used an $8 \times 16 \times 1$ ($6 \times 6 \times 1$) Monkhorst-Pack k-point mesh for unit cell (supercell) calculations. A vacuum of 30 Å along the direction perpendicular to the surface was used to avoid artificial interaction between periodic images, but dipole correction was not considered since the effect of the dipole would not change the adsorption-dependent in-plane quantum transport through the 2D material SnP_3.

The geometries were relaxed to 10^{-4} eV and 0.01 eV per Å for the electronic energy and total atomic force convergence, respectively. The adsorption energies were calculated as follows:

$$E_{ads} = E_{SnP_3+gas} - E_{SnP_3} - E_{gas} - E_{cc} \quad (3)$$

where E_{ads} denotes the adsorption energy, while E_{SnP_3+gas}, E_{SnP_3}, and E_{gas} are the total energies of the system, the substrate, and the gas molecule, respectively. Here, $E_{cc} = E_{SnP_3+ghost states} + E_{gas+ghost states} - (E_{SnP_3} + E_{gas})$ refers to the counterpoise correction to correct the basis set superposition error which may occur due to incompleteness of the basis sets in calculating the interaction energies. The term $E_{SnP_3+ghost states}$ represents the total energy of substrate in the presence of the basis functions on the gas molecule and conversely for $E_{gas+ghost states}$[51].

The single-material device was constructed from metallic left and right electrodes based on 3L SnP_3 and a scattering region based on 1L SnP_3. The difference between the lattice constants of the 3L and 1L was ~2.4 %, so we used that of the latter for the whole device, with no significant change in the electronic properties of the electrodes, which remained metallic. We used a 2×1 supercell of 3L SnP_3 as electrodes, with an additional 2×1 overlap region as a buffer, and a 2×5 supercell of 1L SnP_3 as the transport channel (313-junction). For comparison, we also constructed a model with electrodes (2×3 supercell) and a transport channel (2×6 supercell) made of 1L SnP_3 (111-junction).

Quantum transport calculations

Quantum transport calculations were performed using NEGF theory as implemented in the TranSIESTA code[52]. The transmission function, $T(E)$, is written as:

$$T(E,V) = Tr\left[\Gamma_L(E,V)G(E,V)\Gamma_R(E,V)G^\dagger(E,V)\right] \quad (4)$$

where $\Gamma_L(\Gamma_R)$, G, and V are the broadening matrix of the left (right) electrode, Green's function, and the bias voltage, respectively. The current-voltage (I–V) characteristics were obtained using TBtrans code based on the Landauer-Büttiker formula[46]:

$$I(V) = \frac{2e^2}{h} \int (f_L(E) - f_R(E)) T(E,V) dE \quad (5)$$

where e, h, and f are the electron charge, Planck's constant, and Fermi-Dirac distribution function, respectively. The applied bias, V, can be thought of as the chemical potential difference between the two electrodes divided by the electron charge, $\frac{\mu_L - \mu_R}{e}$. The Fermi-Dirac distribution function of the electrode left/right lead (L/R) is written as $f_{L/R} = \frac{1}{e^{(E-\mu_{L/R})/k_BT}+1}$, where k_B is Boltzmann's constant and T is the electronic temperature.

REFERENCES
1. Lobert, J. M., Scharffe, D. H., Hao, W. M. & Crutzen, P. J. Importance of biomass burning in the atmospheric budgets of nitrogen-containing gases. *Nature* **346**, 552–554 (1990).
2. Zampolli, S. et al. An electronic nose based on solid state sensor arrays for low-cost indoor air quality monitoring applications. *Sens. Actuators B Chem.* **101**, 39–46 (2004).
3. Takahashi, T. et al. Carbon nanotube active-matrix backplanes for mechanically flexible visible light and X-ray imagers. *Nano Lett.* **13**, 5425–5430 (2013).
4. Kim, E. et al. Pattern recognition for selective odor detection with gas sensor arrays. *Sensors* **12**, 16262–16273 (2012).
5. Hagleitner, C. et al. Smart single-chip gas sensor microsystem. *Nature* **414**, 293–296 (2001).
6. Modi, A., Koratkar, N., Lass, E., Wei, B. & Ajayan, P. M. Miniaturized gas ionization sensors using carbon nanotubes. *Nature* **424**, 171–174 (2003).

7. Hodgkinson, J. & Tatam, R. P. Optical gas sensing: a review. *Meas. Sci. Technol.* **24**, 012004 (2012).

8. Dey, A. Semiconductor metal oxide gas sensors: a review. *Mater. Sci. Eng. B* **229**, 206–217 (2018).

9. Late, D. J. et al. Sensing behavior of atomically thin-layered MoS₂ transistors. *ACS Nano* **7**, 4879–4891 (2013).

10. Baugher, B. W. H., Churchill, H. O. H., Yang, Y. & Jarillo-Herrero, P. Intrinsic electronic transport properties of high-quality monolayer and bilayer MoS₂. *Nano Lett.* **13**, 4212–4216 (2013).

11. Lee, K., Gatensby, R., McEvoy, N., Hallam, T. & Duesberg, G. S. High-performance sensors based on molybdenum disulfide thin films. *Adv. Mater.* **25**, 6699–6702 (2013).

12. Mir, S. H., Yadav, V. K. & Singh, J. K. Recent advances in the carrier mobility of two-dimensional materials: a theoretical perspective. *ACS Omega* **5**, 14203–14211 (2020).

13. Roy, P. K., Luxa, J. & Sofer, Z. Emerging pnictogen-based 2D semiconductors: sensing and electronic devices. *Nanoscale* **12**, 10430–10446 (2020).

14. Splendiani, A. et al. Emerging photoluminescence in monolayer MoS₂. *Nano Lett.* **10**, 1271–1275 (2010).

15. Ramzan, M. S., Bacic, V., Jing, Y. & Kuc, A. Electronic properties of a new family of layered materials from groups 14 and 15: first-principles simulations. *J. Phys. Chem. C.* **123**, 25470–25476 (2019).

16. Jing, Y., Ma, Y., Li, Y. & Heine, T. GeP₃: a small indirect band gap 2D crystal with high carrier mobility and strong interlayer quantum confinement. *Nano Lett.* **17**, 1833–1838 (2017).

17. Liu, H. et al. Phosphorene: an unexplored 2D semiconductor with a high hole mobility. *ACS Nano* **8**, 4033–4041 (2014).

18. Bhimanapati, G. R. et al. Recent advances in two-dimensional materials beyond graphene. *ACS Nano* **9**, 11509–11539 (2015).

19. Babar, V., Sharma, S. & Schwingenschlögl, U. New paradigm for gas sensing by two-dimensional materials. *J. Phys. Chem. C.* **123**, 13104–13109 (2019).

20. Babar, V., Vovusha, H. & Schwingenschlögl, U. Density functional theory analysis of gas adsorption on monolayer and few layer transition metal dichalcogenides: implications for sensing. *ACS Appl. Nano Mater.* **2**, 6076–6080 (2019).

21. Thomas, S., Kumar, V., Roy, D. R. & Zaeem, M. A. Two-dimensional boron–phosphorus monolayer for reversible NO₂ gas sensing. *ACS Appl. Nano Mater.* **3**, 10073–10081 (2020).

22. Li, H. et al. Fabrication of single- and multilayer MoS₂ film-based field-effect transistors for sensing NO at room temperature. *Small* **8**, 63–67 (2012).

23. Sharma, M., Jamdagni, P., Kumar, A. & Ahluwalia, P. K. Interactions of gas molecules with monolayer MoSe₂: a first principle study. *AIP Conf. Proc.* **1731**, 140045 (2016).

24. Bui, V. Q., Pham, T.-T., Le, D. A., Thi, C. M. & Le, H. M. A first-principles investigation of various gas (CO, H₂O, NO, and O₂) absorptions on a WS₂ monolayer: stability and electronic properties. *J. Phys. Condens. Matter* **27**, 305005 (2015).

25. Shaheen, A., Ali, M., Othman, W. & Tit, N. Origins of negative differential resistance in N-doped ZnO nano-ribbons: ab-initio investigation. *Sci. Rep.* **9**, 9914 (2019).

26. Fan, S. et al. Tunable negative differential resistance in van der Waals heterostructures at room temperature by tailoring the interface. *ACS Nano* **13**, 8193–8201 (2019).

27. Das, S. & Appenzeller, J. WSe₂ field effect transistors with enhanced ambipolar characteristics. *Appl. Phys. Lett.* **103**, 103501 (2013).

28. Large, L. N. & Bicknell, R. W. Ion-implantation doping of semiconductors. *J. Mater. Sci.* **2**, 589–609 (1967).

29. Gong, C., Colombo, L., Wallace, R. M. & Cho, K. The unusual mechanism of partial Fermi level pinning at metal–MoS₂ interfaces. *Nano Lett.* **14**, 1714–1720 (2014).

30. Tung, R. T. The physics and chemistry of the Schottky barrier height. *Appl. Phys. Rev.* **1**, 011304 (2014).

31. Yang, L. et al. Chloride molecular doping technique on 2D materials: WS₂ and MoS₂. *Nano Lett.* **14**, 6275–6280 (2014).

32. Andrews, K., Bowman, A., Rijal, U., Chen, P.-Y. & Zhou, Z. Improved contacts and device performance in MoS₂ transistors using a 2D semiconductor interlayer. *ACS Nano* **14**, 6232–6241 (2020).

33. Kappera, R. et al. Phase-engineered low-resistance contacts for ultrathin MoS₂ transistors. *Nat. Mater.* **13**, 1128–1134 (2014).

34. Ghorbani-Asl, M., Kuc, A., Miró, P. & Heine, T. A single-material logical junction based on 2D crystal PdS₂. *Adv. Mater.* **28**, 853–856 (2016).

35. Sajjad, M., Montes, E., Singh, N. & Schwingenschlögl, U. Superior gas sensing properties of monolayer PtSe₂. *Adv. Mater. Interfaces* **4**, 1600911 (2017).

36. Su, T.-Y. et al. Highly sensitive, selective and stable NO₂ gas sensors with a ppb-level detection limit on 2D-platinum diselenide films. *J. Mater. Chem. C.* **8**, 4851–4858 (2020).

37. Sun, S., Meng, F., Wang, H., Wang, H. & Ni, Y. Novel two-dimensional semiconductor SnP₃: high stability, tunable bandgaps and high carrier mobility explored using first-principles calculations. *J. Mater. Chem. A* **6**, 11890–11897 (2018).

38. Tian, R. et al. Liquid exfoliated SnP₃ nanosheets for very high areal capacity lithium-ion batteries. *Adv. Energy Mater.* **11**, 2002364 (2021).

39. Chaves, A. et al. Bandgap engineering of two-dimensional semiconductor materials. *npj 2D Mater. Appl* **4**, 1–21 (2020).

40. Miró, P., Ghorbani-Asl, M. & Heine, T. Two dimensional materials beyond MoS₂: noble-transition-metal dichalcogenides. *Angew. Chem. Int. Ed.* **53**, 3015–3018 (2014).

41. Hulliger, F. *Structural Chemistry of Layer-Type Phases* (Springer Science & Business Media, 2012).

42. Peng, S., Cho, K., Qi, P. & Dai, H. Ab initio study of CNT NO₂ gas sensor. *Chem. Phys. Lett.* **387**, 271–276 (2004).

43. Li, X., Li, X., Li, Z., Wang, J. & Zhang, J. WS₂ nanoflakes based selective ammonia sensors at room temperature. *Sens. Actuators B Chem.* **240**, 273–277 (2017).

44. Chinh, N. D. et al. NO gas sensing kinetics at room temperature under UV light irradiation of In₂O₃ nanostructures. *Sci. Rep.* **6**, 35066 (2016).

45. Zhou, T. & Zhang, T. Recent progress of nanostructured sensing materials from 0D to 3D: overview of structure-property-application relationship for gas sensors. *Small Methods* **5**, 2100515 (2021).

46. Papior, N. R., Lorente, N., Frederiksen, T., García, A. & Brandbyge, M. Improvements on non-equilibrium and transport green function techniques: the next-generation TRANSIESTA. *Comput. Phys. Commun.* **212**, 8–24 (2017).

47. Gullman, J. & Olofsson, O. The crystal structure of SnP₃ and a note on the crystal structure of GeP₃. *J. Solid State Chem.* **5**, 441–445 (1972).

48. Soler, J. M. et al. SIESTA method for ab initio order-N materials simulation. *J. Phys. Condens. Matter* **14**, 2745–2779 (2002).

49. Troullier, N. & Martins, J. L. Efficient pseudopotentials for plane-wave calculations. *Phys. Rev. B* **43**, 1993–2006 (1991).

50. Perdew, J. P., Burke, K. & Ernzerhof, M. Generalized gradient approximation made simple. *Phys. Rev. Lett.* **77**, 3865–3868 (1996).

51. Boys, S. F. & Bernardi, F. The calculation of small molecular interactions by the differences of separate total energies. Some procedures with reduced errors. *Mol. Phys.* **19**, 553–566 (1970).

52. Brandbyge, M., Mozos, J.-L., Ordejón, P., Taylor, J. & Stokbro, K. Density-functional method for nonequilibrium electron transport. *Phys. Rev. B* **65**, 165401 (2002).

ACKNOWLEDGEMENTS

AUTHOR CONTRIBUTIONS

M.S.R. and H.S.K. conceived the research; M.S.R. conducted the first-principles calculations; A.B.K. and H.S.K. analysed the data and supervised the work. All authors contributed to the discussions and wrote the manuscript together.

COMPETING INTERESTS

The authors declare no competing interests.

ADDITIONAL INFORMATION

Supplementary information The online version contains supplementary material available at https://doi.org/10.1038/s41524-022-00903-7.

Correspondence and requests for materials should be addressed to Agnieszka B. Kuc or Han Seul Kim.

Reprints and permission information is available at http://www.nature.com/reprints

Publisher's note Springer Nature remains neutral with regard to jurisdictional claims in published maps and institutional affiliations.